HiSST: 3rd International Conference on
High-Speed Vehicle Science Technology
14 -19 April 2024, Busan, Korea

Mechanisms for Combustion Instability by Micro-Rocket Torch in Scramjet Combustor based on Dynamic Mode Decomposition

Shinichiro Ogawa[1]

Abstract

To achieve ignition and stable combustion within a short residence time of milliseconds, the effective stabilization of flames in scramjet combustors is crucial. Stable forced ignition and flame holding have been explored in previous studies using various igniters, including micro-rocket torches and plasma jet torches. In this study, the forced ignition and combustion instability of a scramjet combustor equipped with a micro-rocket torch are investigated. Despite successful ignition promoted by the micro-rocket torch in previous experiments, combustion instabilities were observed in the cavity flame holder, as revealed by OH* chemiluminescence images. To elucidate the mechanisms of forced ignition and combustion instability, modal analysis techniques, specifically dynamic mode decomposition (DMD), are employed. DMD is a powerful method for extracting spatiotemporally coherent structures from high-dimensional data, making it suitable for analysing combustion dynamics. DMD was applied to OH* chemiluminescence images obtained from previous supersonic combustion experiments. The dominant modes associated with combustion instability are identified, and their spectral characteristics are investigated via power spectrum density (PSD) analysis. From the results, it is clarify the combustion instability near the cavity flame holder, (a) in the case of low frequencies between 100 to 400 Hz were formed by fuel injector flame feedback in this combustion result, (b) in the case of low frequencies under 100 Hz (e.g., 15 to 50 Hz) were formed by torch gas injector flame feedback in this combustion result, and (c) in the case of high frequencies over 1000 Hz were formed by interference between the cavity flame holder and the flow field. Insights into the complex flow dynamics within the cavity flame holder and the shear layer are provided, shedding light on the mechanisms underlying combustion instability in scramjet engines equipped with micro-rocket torches.

Keywords: Dynamic Mode Decomposition, Scramjet Combustor, Cavity Flameholder, Micro-Rocket Torch, Combustion Instability

Nomenclature

$\mathbf{A}$	Matrix for system of equations or dynamics
$\tilde{\mathbf{A}}$	Reduced dynamics on the r-dimensional POD subspace
t	Time
$\tilde{\mathbf{U}}$	Left singular vectors of the truncated SVD of $\mathbf{X}$, $\mathbf{U} \in \mathbb{R}^{n \times r}$
$\tilde{\mathbf{V}}$	Right singular vectors of the truncated SVD of $\mathbf{X}$, $\mathbf{V} \in \mathbb{R}^{m \times r}$
$\tilde{\mathbf{\Sigma}}$	Matrix of singular values of the truncated SVD of $\mathbf{X}$, $\Sigma \in \mathbb{R}^{r \times r}$
$\mathbf{W}$	Eigenvectors of $\tilde{\mathbf{A}}$
$\mathbf{x}$	state of a system, $\mathbf{x} \in \mathbb{R}^{n}$
$\tilde{\mathbf{x}}$	Reduced state, $\tilde{\mathbf{x}} \in \mathbb{R}^{r}$
$\mathbf{x}_k$	Snapshot of data at time t_k
$\mathbf{X}$	Data matrix, $\mathbf{X} \in \mathbb{R}^{n \times m}$
$\mathbf{X'}$	Time-shifted data matrix, $\mathbf{X}' \in \mathbb{R}^{n \times m}$

[1] *Osaka Metropolitan University, 1-1, Gakuen-cho, Naka-ku, Sakai, Osaka 599-8531, Japan, shinichiro.ogawa@omu.ac.jp*

$\mathbf{\Lambda}$	Diagonal matrix of eigenvalues	$\|\cdot\|_F$	Frobenius norm of a matrix $\mathbf{X}$
$\mathbf{\Phi}$	Matrix of DMD modes		

1. Introduction

Effective flame stabilization in the scramjet combustor is required to complete ignition and stable combustion in a short residence time on the order of milliseconds. In a previous study, we investigated stable forced ignition and flame holding in a scramjet combustor using a micro-rocket torch [1-3]. Furthermore, many researchers have investigated various igniters, including plasma jet torches [4, 5], pulse detonators [6], and lasers [7]. in previous studies. The micro-rocket torch can promote ignition by injecting combustion gas directly into the combustor. Kobayashi et al. [1] reported that sufficient promotion of ignition can be achieved not only by a plasma jet torch but also by a micro-rocket torch [1]. In our previous combustion experiments [2], the micro-rocket torch sufficiently promoted ignition in the cavity flame holder. However, forced ignition and combustion instabilities in the cavity flame holder were observed from the OH* chemiluminescence image. It is difficult to clarify the forced ignition and combustion instability mechanisms using an enormous quantity of image data. Furthermore, combustion instabilities inevitably occur in the highly turbulent combustion of scramjets. Combustion instability causes many undesirable features in scramjet engines, such as (1) large amplitude acoustic oscillation and (2) mechanical vibrations of the combustor and other systems in the engine [8, 9]. Therefore, it is necessary to clarify the combustion instability for stable operation of scramjet engines.

To investigate the forced ignition and combustion instability mechanisms using an enormous quantity of OH* chemiluminescence image data, modal analysis was the focus of this study. Proper orthogonal decomposition (POD) and dynamic mode decomposition (DMD) have become popular in modal analysis. POD is a modal decomposition technique that extracts modes based on optimizing the mean square of the field variable being examined [10]. The advantages of POD are its abundantly clear theory and its better interpretability of the extracted parameters. However, the disadvantages of POD are that it is less descriptive due to the simplicity of the modal structure and its loss of generality depending on the original data. DMD provides a means to decompose time-resolved data into modes, with each mode having a single characteristic frequency of oscillation and growth/decay rate [10]. The advantages of the DMD are its greater ability to extract features from time series data of phenomena, including vibration, and its easy semantic interpretation when assumed to be a superposition of pure vibration. Therefore, to clarify the forced ignition and combustion instabilities, modal analysis using DMD, which has a greater ability to extract features from time series data of phenomena, including vibration, was the focus of this study.

DMD was developed by Schmid [11] to identify spatiotemporally coherent structures from high dimensional fluid phenomenon data. In a previous study, DMD was applied to three-dimensional jet-in-cross flow numerical simulation data and cavity flow experimental data [11, 12]. According to Schmid [11], DMD has proven to be a robust and reliable algorithm for extracting spatiotemporally coherent structures from data based on the validation results of a variety of flow models. Furthermore, in supersonic combustion studies, flame instability has been widely studied using DMD [8, 13-17]. In previous studies, the supersonic combustion instability at the cavity [13, 14], isolator [15, 16], strut [17], and wall jet [8] was investigated using the DMD. According to previous studies, DMD reveals the modes responsible for the peak amplitude in the noise in scramjet combustors with passive struts [17]. The data-driven approach with SP-DMD clarifies the combustion instability mechanism of supersonic combustion in detail [13]. However, the forced ignition and combustion instability mechanisms of the micro-rocket torch in the cavity using the DMD were unclear. To our knowledge, few studies have reported dynamic mode results for ignition and combustion instability in a scramjet engine using a torch.

The aim of this study was to clarify the combustion instability of a micro-rocket torch installed in a scramjet combustor using a DMD. The DMD was applied to OH* chemiluminescence images measured by our previous supersonic combustion experiments [2, 3]. A supersonic combustion experimental study was conducted on different cavity configurations and different fuel mass flow rates. The paper is organized as follows: In Sec. 2, the combustion experimental setup is described. The dynamic mode decomposition procedure is described in Sec. 3. The effects of different fuel mass flow rates on the forced ignition instability and combustion instability using the DMD are described in Sec. 4.

2. Combustion experimental setup

2.1. Scramjet combustor and micro-rocket torch

Combustion experiments were performed in a basic combustion wind tunnel test facility at the Kakuda Space Center of the Japan Aerospace Exploitation Agency (JAXA) in Miyagi, Japan. Detailed information on the combustion test facility can be found in a previous paper [18]. The basic combustion wind tunnel test facility is a directly connected combustion facility. This test facility consists of a Mach 2.5 nozzle, a constant-area isolator, a constant area section combustor, and a one-sided divergent section combustor, as shown in Fig. 1.

There is a window in the region framed by red dashed lines through which the ignition and combustion phenomenon can be optically accessed. A quartz window was installed on the sidewalls in a constant area section with a length and width of 300 mm and 70 mm, respectively. The length and width of this window are 320 mm and 96 mm, respectively.

The combustion experiment was conducted under the conditions of a mainstream Mach number of 2.5, a mainstream total temperature of 1833 K, and a mainstream total pressure of 1.0 MPa. The total temperature of the mainstream was controlled by a vitiation air heater [19]. This heater generated a high-temperature flow by the lean burning of hydrogen. The main airflow contained H2O; for example, the mole fraction of H2O was 0.232 for the total temperature of the main airflow of 1833 K. In this experiment, a fuel mixture consisting of 36% methane and 64% ethylene was used.

As shown in Figs. 1 (b) and (c), a micro-rocket torch is installed on the bottom surface 5.0 mm downstream from the step of the cavity flame holder. This torch serves as an igniter by injecting combustion gas into the mainstream to promote ignition. In this study, combustion gas consisting of hydrogen and oxygen with an equivalence ratio of 2.0 is injected from the torch into the cavity flame holder. The micro-rocket torch has a length of 183 mm, and it contains a cylindrical combustion chamber with a diameter of 10 mm. Inside the combustion chamber, a spark plug is installed to ignite the mixture of hydrogen and oxygen. The nozzle diameter of this torch is 2.5 mm. The combustion gas temperature was 1400 K for this torch setup.

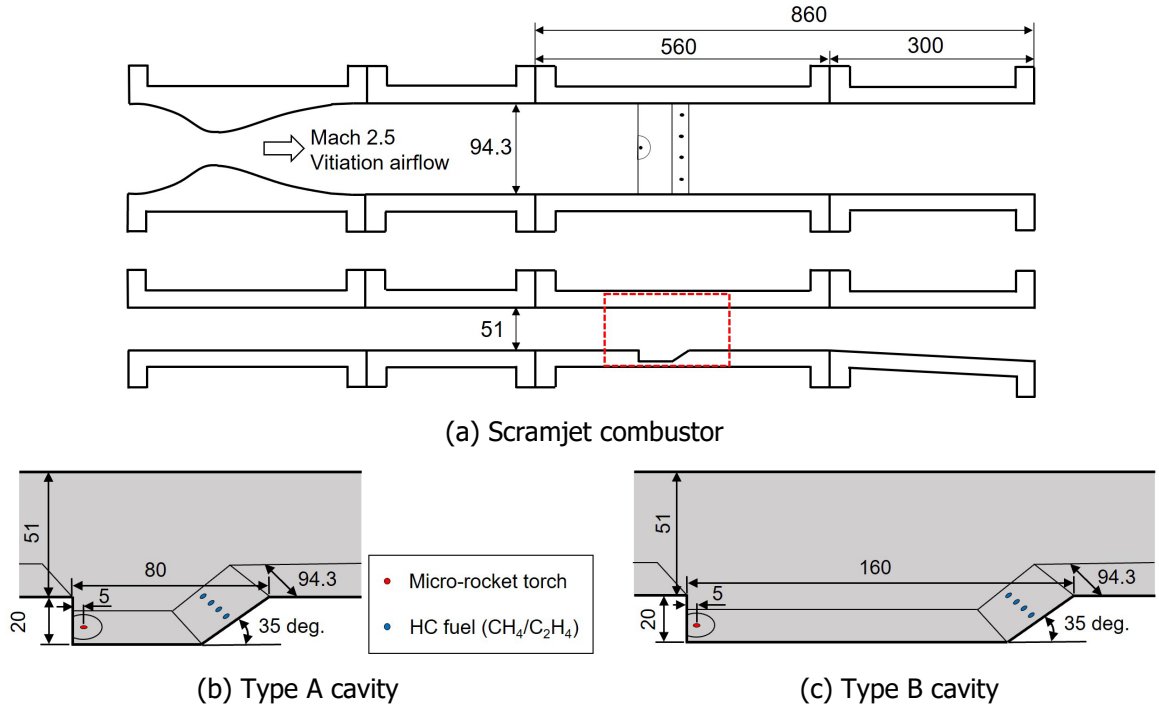

Fig 1. Detailed illustration of the scramjet combustor and two types of cavity flame holders.

The duration of the experiment in this study was 45 seconds. Within this time frame, combustion experiments were conducted with fuel injection for only 5 seconds, forced ignition using a micro-rocket torch for 4 seconds, and flame holding after torch cessation for 2 seconds. The results of the combustion experiments are presented in Table 1. In the Type-A cavity, combustion experiments were conducted at two fuel mass flow rates: 2.3 g/s and 5.4 g/s. In the Type-B cavity, combustion experiments were conducted at four fuel flow mass rates ranging from 4.7 g/s to 30.3 g/s. From the combustion experiment results, self-ignition was not achieved under any conditions for either Type-A or Type-B cavities. On the other hand, forced ignition using the micro-rocket torch was achieved under all conditions. Flame holding was achieved for Type-A at a fuel mass flow rate of 2.3 g/s and for Type-B at fuel mass flow rates of 4.7 g/s and 30.3 g/s.

Table 1. Summary of the combustion experiment results.

No.	Cavity type	Fuel mass flow rate, g/s	Self-ignition	Forced ignition	Flame holdings
A-1	Type A	2.3	NO	YES	YES
A-2		5.4	NO	YES	NO
B-1	Type B	4.7	NO	YES	YES
B-2		10.2	NO	YES	NO
B-3		19.3	NO	YES	NO
B-4		30.3	NO	YES	YES

2.2. Optical diagnostic system

To visualize the ignition, combustion, and flame holding process in the cavity, we used a high-speed camera. A schematic of the optical diagnostic system is shown in Fig. 2. A high-speed camera (FASTCAM SA5, Photron) was used to capture OH* chemiluminescence images. The luminosity of OH* was imaged using band-pass filter (Semrock) with a ±20 nm bandwidth interference filter centered at 320 nm. The camera was fitted with a f4.5/105 mm UV Nikkor lens (Nikon), image intensifier (C10880-03F, Hamamatsu Photonics), and relay lens (A2098, Hamamatsu Photonics). The frame rate of the high-speed camera was set at 7,000 fps in the case of a Type-A cavity, and at 10,000 fps in the case of a Type-B cavity, with a resolution of 512 pixels by 300 pixels. OH chemiluminescence was measured for 5 seconds from ignition to flame holding.

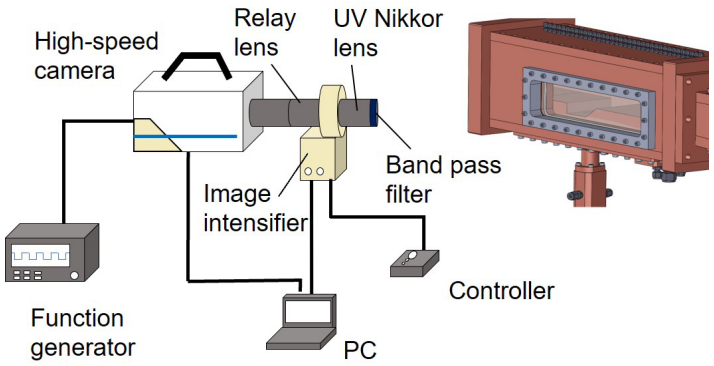

Fig 2. Schematics of optical diagnostic system.

3. Dynamic mode decomposition (DMD)

In this study, mode analysis using Dynamic Mode Decomposition (DMD) was conducted. DMD is a versatile matrix decomposition method that leverages the power of singular value decomposition (SVD). Mode analysis using DMD was performed with reference to the DMD algorithm by Kutz et al. [20] and Brunton et al. [21]. Furthermore, when analysis the temporal evolution of OH* chemiluminescence image data in a grid-like spatial domain, using a snapshot-based approach proves to be effective. An overview of the modal analysis procedure using DMD is shown in Fig. 3.

A snapshot may indicate that the state of a system is reshaped into a high-dimensional column vector. First, the snapshot data are arranged into two data matrices (**X** and **X'**).

$$\mathbf{X} = \begin{bmatrix} | & | & & | \\ \mathbf{x}(t_1) & \mathbf{x}(t_2) & \cdots & \mathbf{x}(t_m) \\ | & | & & | \end{bmatrix} \tag{1}$$

$$\mathbf{X}' = \begin{bmatrix} | & | & & | \\ \mathbf{x}(t_1') & \mathbf{x}(t_2') & \cdots & \mathbf{x}(t_m') \\ | & | & & | \end{bmatrix} \tag{2}$$

The DMD algorithm seeks to find the leading spectral decomposition of linear operator **A** that best relates two snapshot matrices temporally.

$$\mathbf{X}' \approx \mathbf{A}\mathbf{X} \tag{3}$$

Temporally uniform sampling can be expressed as follows: $\mathbf{x}_{k+1} \approx \mathbf{A}\mathbf{x}_k$. The best fit operator **A** is defined as follows.

$$\mathbf{A} = \arg\min_{\mathbf{A}} \left\| \mathbf{X}' - \mathbf{A}\mathbf{X} \right\|_F = \mathbf{X}'\mathbf{X}^{\dagger} \tag{4}$$

First, the singular value decomposition of **X** is computed as follows.

$$\mathbf{X} \approx \tilde{\mathbf{U}} \tilde{\Sigma} \tilde{\mathbf{V}}^* \tag{5}$$

Next, the full matrix **A** may be obtained by using the pseudo inversed of **X** obtained via singular value decomposition.

$$\mathbf{A} = \mathbf{X}'\tilde{\mathbf{V}} \tilde{\Sigma}^{-1} \tilde{\mathbf{U}}^* \tag{6}$$

$\tilde{\mathbf{A}}$, which was the r × r projection of the full matrix A onto POD modes, was calculated as follows.

$$\tilde{\mathbf{A}} = \tilde{\mathbf{U}}^* \mathbf{A} \tilde{\mathbf{U}} = \tilde{\mathbf{U}}^* \mathbf{X}' \tilde{\mathbf{V}} \tilde{\Sigma}^{-1} \tag{7}$$

It is important to note that the reduced matrix $\tilde{\mathbf{A}}$ has the same nonzero eigenvalues as the full matrix **A**. The reduced order matrix $\tilde{\mathbf{A}}$ defines a linear model for the dynamics of the vector of POD coefficients $\tilde{\mathbf{x}}$ as follows.

$$\tilde{\mathbf{x}}_{k+1} = \tilde{\mathbf{A}} \tilde{\mathbf{x}}_k \tag{8}$$

The spectral decomposition of $\mathbf{\Lambda}$ was performed as follows.

$$\tilde{\mathbf{A}}\mathbf{W} = \mathbf{W}\mathbf{\Lambda} \tag{9}$$

Finally, the high dimensional DMD mode $\mathbf{\Phi}$ is reconstructed using the eigenvectors **W** of the reduced system and the time-shifted snapshot matrix **X'**.

$$\mathbf{\Phi} = \mathbf{X}'\tilde{\mathbf{V}} \tilde{\Sigma}^{-1} \mathbf{W} \tag{10}$$

According to Tu et al. [22], these DMD modes are eigenvectors of the high dimensional **A** matrix corresponding to the eigenvalues in $\mathbf{\Lambda}$.

$$\begin{aligned}\mathbf{A\Phi} &= \left(\mathbf{X'}\tilde{\mathbf{V}}\tilde{\Sigma}^{-1}\tilde{\mathbf{U}}^{*}\right)\left(\mathbf{X'}\tilde{\mathbf{V}}\tilde{\Sigma}^{-1}\mathbf{W}\right)\\ &= \mathbf{X'}\tilde{\mathbf{V}}\tilde{\Sigma}^{-1}\tilde{\mathbf{A}}\mathbf{W}\\ &= \mathbf{X'}\tilde{\mathbf{V}}\tilde{\Sigma}^{-1}\mathbf{W}\mathbf{\Lambda}\\ &= \mathbf{\Phi\Lambda}\end{aligned} \tag{11}$$

In this study, the modal analysis code using DMD was written in the MATLAB.

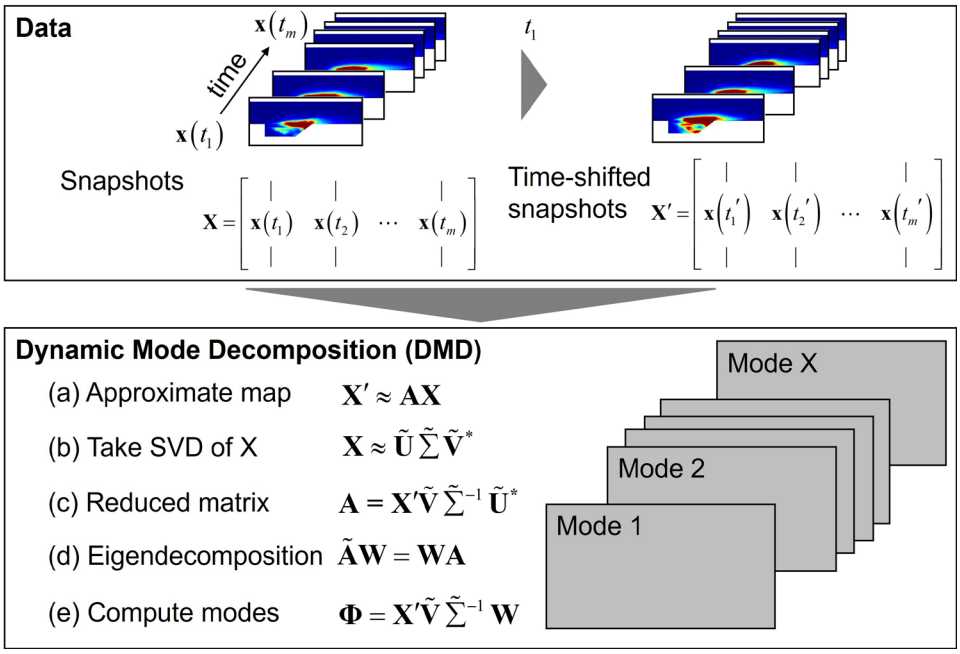

Fig 3. Data processing in dynamic mode decomposition.

4. Results and discussion

4.1. Combustion performance within the cavity flame holder

Figure 4 shows the wall pressure distribution and mean OH* chemiluminescence images for the Type-A cavity. The horizontal axis represents the length of the constant section, while the vertical axis represents the normalized wall pressure at each measurement position. The normalized wall pressure is normalized by the mainstream pressure. As a reference, a sketch of the model combustor wall (cavity side) is overlaid with solid black lines. In addition, this figure shows the mean OH* chemiluminescence images for A-1 and A-2. These images are obtained by averaging over a duration of 4 seconds (28,000 images) during the forced ignition.

In the case of Type-A, the pressure distribution near the cavity flame holder remains largely unchanged with increasing fuel mass flow rate. However, downstream of the cavity flame holder, the pressure profile slightly increases with increasing fuel flow rate. The difference can be confirmed by the average OH* chemiluminescence images. As shown in the OH* chemiluminescence average images in Figs. 4(c) and (d), in the case of A-1, a combustion region is formed inside the cavity flame holder, whereas in the case of A-2, a combustion region is formed downstream from the cavity lamp. Therefore, in the case of the Type-A cavity, an increase in the fuel mass flow rate leads to the migration of the combustion region from inside the cavity flame holder towards the downstream side.

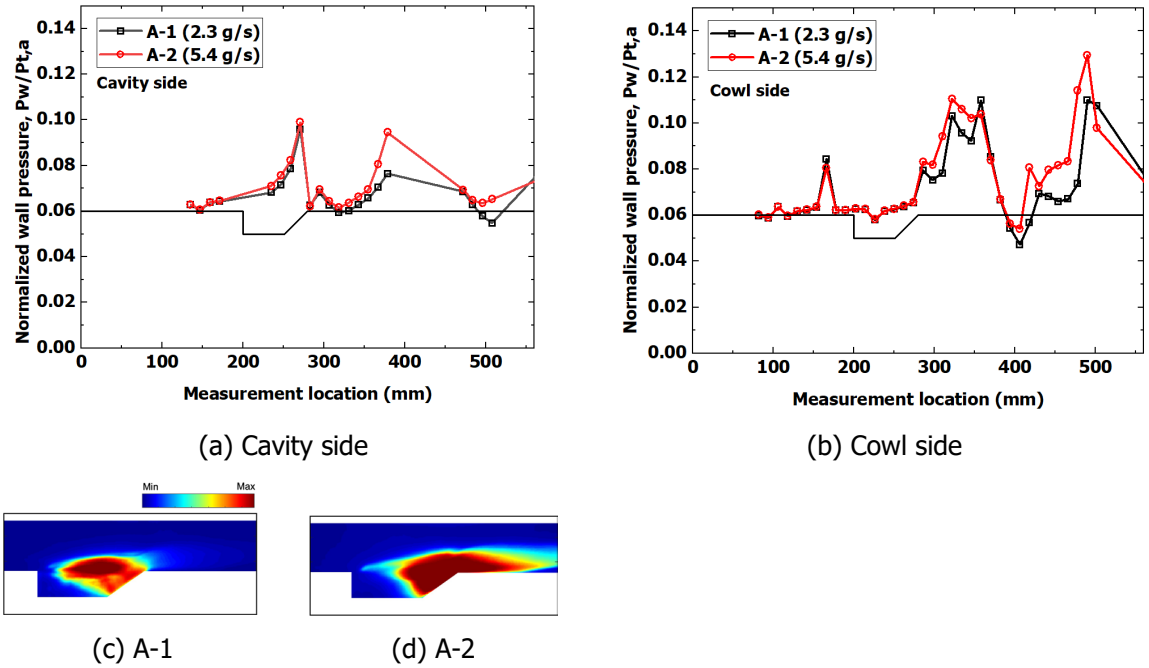

(a) Cavity side (b) Cowl side

(c) A-1 (d) A-2

Fig 4. Wall pressure distributions and mean OH* chemiluminescence images for Type-A cavity.

Figure 5 shows the wall pressure distribution for the Type-B cavity. In addition, this figure shows the mean OH* chemiluminescence images for B-1, B-2, B-3, and B-4. These images are obtained by averaging over a duration of 4 seconds (40,000 images) during the forced ignition. In the case of B-1 and B-2 at the cavity side (see Fig. 5 (a)), the pressure distribution near the cavity flame holder remains largely unchanged with increasing fuel mass flow rate. On the other hand, on the cowl side (see Fig. 5 (b)), the pressure profile slightly increases at the cavity ramp compared with B-1 and B-2. The difference can be confirmed by the average OH* chemiluminescence images. As shown in Figs. 5 (c) and (d), in the case of A-1, a combustion region is formed inside the cavity flame holder, whereas in the case of A-2, a combustion region is formed from the shear layer downstream from the cavity ramp. The wall pressure at the cavity side of B-3 becomes higher than that of B-1 and B-2. Furthermore, in the case of B-3, the pressure on the cowl side was higher than that on the cavity side. The pressure distribution on the cowl side exhibits a waveform resembling that of periodic waves. As shown in Fig. 5 (e), flames are formed from the cavity step, and OH* chemiluminescence is observed behind the cavity flame holder from the shear layer to the mainstream. Additionally, in the case of B-3, flame flickering is observed. In the case of B-4, the pressure in all regions becomes higher than that of the other fuel mass flow rates. Furthermore, in this case, a part of the recirculating flow region in the cavity penetrated upstream and downstream beyond the cavity step and ramp because more fuel was supplied and the pressure in the cavity increased. As a result, OH* chemiluminescence was observed throughout the entire flow path, as shown in Fig. 5 (f). Therefore, the combustion characteristics within the cavity flame holder and throughout the flow path vary as the fuel mass flow rate changes.

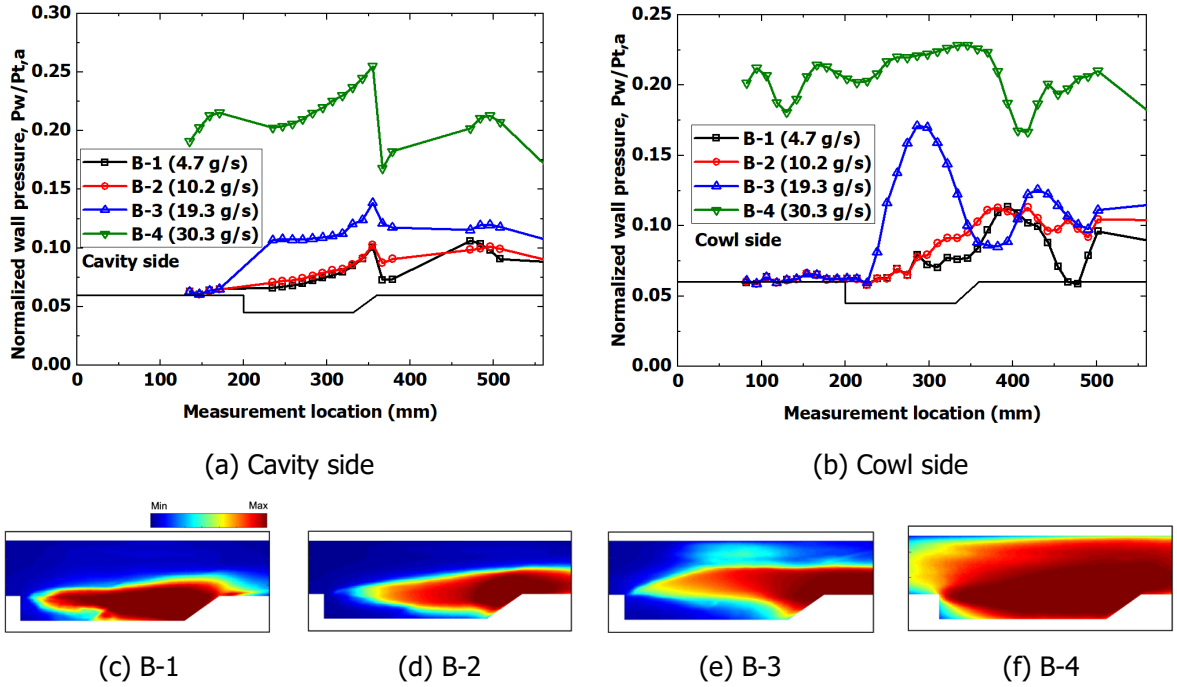

(a) Cavity side (b) Cowl side

(c) B-1 (d) B-2 (e) B-3 (f) B-4

Fig 5. Wall pressure distributions and mean OH* chemiluminescence images for Type-B cavity.

4.2. Combustion instability within the shear layer

Figure 6 shows the time history of the OH* chemiluminescence intensity within the shear layer of the cavity flame holder during forced ignition by the micro-rocket torch. In the case of A-1, slight periodic oscillations are observed near the penetration of torch gas into the shear layer, while stable combustion occurs within the cavity flame holder. Conversely, in the case of A-2, a combustion region extends downstream from the ramp portion of the cavity flame holder, with unstable combustion occurring from the vicinity of the torch gas penetrating into the shear layer to the midsection of the cavity flame holder.

In the case of B-1, combustion remains stable within the cavity flame holder similar to A-1. Additionally, while slight oscillations occur near the penetration of torch gas into the shear layer, they are not periodic unlike in A-1. For B-2 and B-3, combustion extends from the ramp portion of the cavity flame holder downstream, with combustion oscillations occurring within the cavity flame holder for both cases. This phenomenon of flame flickering within the shear layer was also confirmed from the measured OH chemiluminescence data. It can be conjectured that such phenomena occur not only due to the torch gas but also due to the significant influence of the increase in fuel mass flow rate. In the case of B-4, combustion initiates at the cavity ramp within the first few microseconds, but subsequently, the entire flow path from the cavity flame holder becomes a combustion region. Additionally, a slightly unstable combustion region is observed near the step of the cavity flame holder.

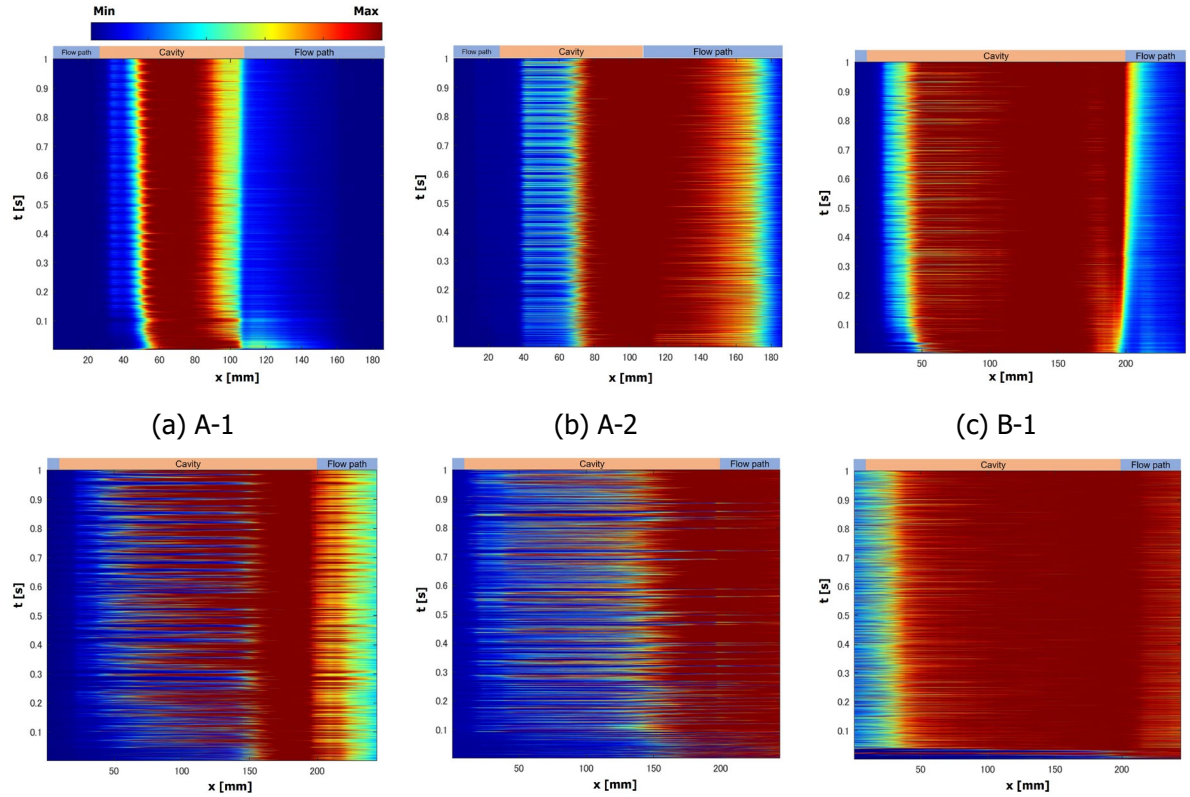

(a) A-1 (b) A-2 (c) B-1

(d) B-2 (e) B-3 (f) B-4

Fig 6. Time history of OH* chemiluminescence intensity within the shear layer of the cavity flameholder during forced ignition by the micro-rocket torch.

Figure 7 shows the time history of the OH* chemiluminescence intensity within the shear layer of the cavity flame holder during flame holding. In the case of A-1, periodic oscillations were observed near the penetration of torch gas into the shear layer during forced ignition, but no oscillations were observed during flame holding, indicating stable combustion within the cavity flame holder. In the case of A-2, as indicated in Table 1, it represents conditions where flame holding was not achieved. Consequently, there is unstable combustion within the cavity flame holder and downstream of the ramp. Therefore, it can be inferred that flame blow-off likely occurs subsequently. Similar to A-1, B-1 exhibits stable combustion within the cavity flame holder, achieving stable flame holding. On the other hand, B-2 and B-3, compared to the forced ignition phase (see Figs. 6(d) and (e)), show the formation of a combustion region within the cavity flame holder at the beginning of flame stabilization. However, after 0.6 s, the combustion region moves to the cavity ramp, followed by flame blow-off. B-4 exhibits a distribution similar to that during forced ignition (see Fig. 6(f)), indicating stable flame holding throughout the entire flow path from the cavity flame holder.

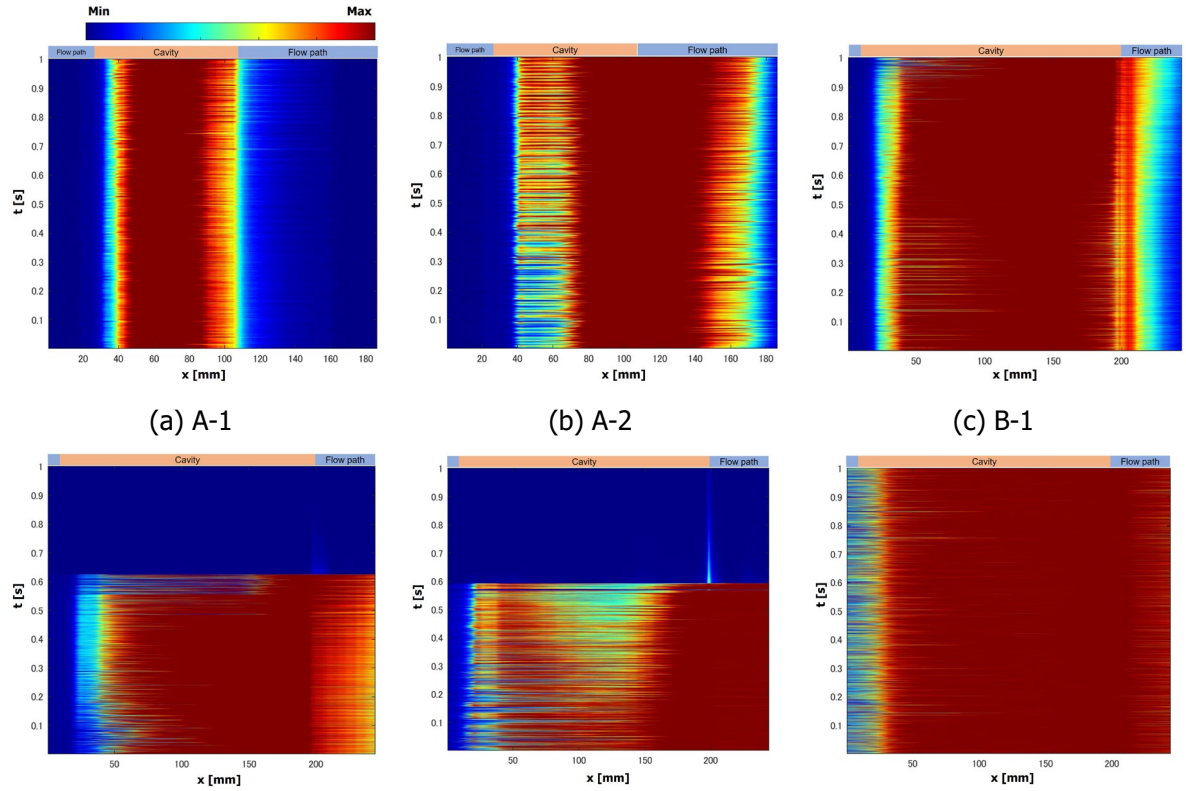

(a) A-1 (b) A-2 (c) B-1

(d) B-2 (e) B-3 (f) B-4

Fig 7. Time history of OH* chemiluminescence intensity within the shear layer of the cavity flameholder during flame holding.

4.3. Effect of different fuel mass flow rates on the combustion instability using the DMD

DMD analysis was conducted using a snapshot-based method with OH* chemiluminescence images. For the Type-A cavity, DMD analysis was performed using a total of 7,000 images. For the Type-B cavity, DMD analysis was performed using a total of 10,000 images. For both Type-A and Type-B cavities, investigations were conducted on forced ignition and combustion instability using data from the first second after the start of forced ignition.

Analysing eigenvalues from Dynamic Mode Decomposition (DMD) results is crucial for understanding the dynamics of a system. By examining eigenvalues extracted from DMD analysis, important information regarding the dynamics of the original data can be obtained, aiding in the evaluation of system stability, behavior, and predictive capabilities. Eigenvalues in the interior of the unit circle and close to the unit circle are characterized as follows [23]: (1) eigenvalues in the interior of the unit circle type correspond to strong damping, and (2) in the case of being close to the unit circle type, all eigenvalues are very close to the unit circle, describing the periodic dynamics of the associated modes. Figure 8 shows the eigenvalues obtained from the DMD algorithm for the Type A and B cavities (A-1 and B-1). Each dot corresponds to one mode. As shown in Fig. 8(a), the eigenvalues are primarily located on the unit circle. This supports the idea that the observed OH* chemiluminescence represents a periodic flow without amplification or decay. Similarly, plotting the eigenvalues obtained from the DMD algorithm for the Type-B cavity results in Fig. 8(b). The eigenvalues are mainly located on the unit circle for the Type-B cavity as well. The OH* chemiluminescence observed in the Type-B cavity represents a periodic flow without amplification or decay, similar to the Type-A cavity. Figure 8 shows the eigenvalues for types A-1 and B-1, but similar results are obtained for other cases as well.

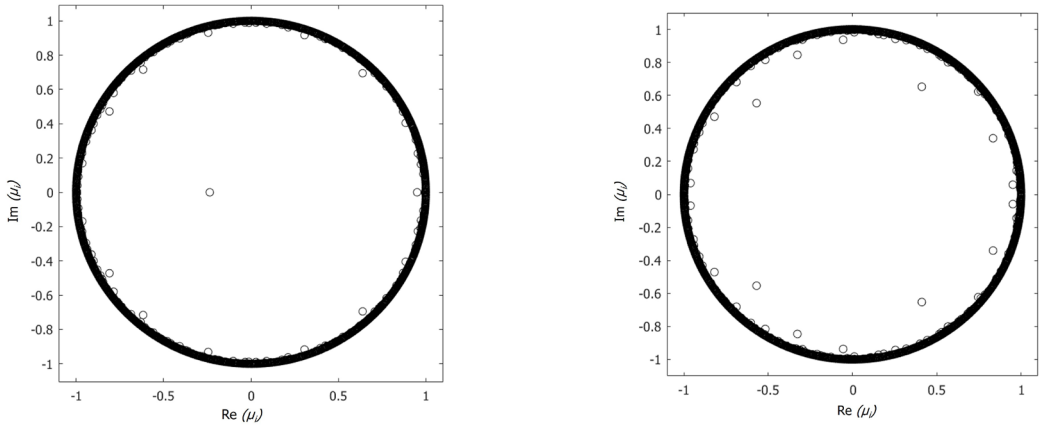

(a) Type-A (A-1) (b) Type-B (B-1)

Fig 8. Eigenvalues found from DMD in types A and B cavity.

The effect of a micro-rocket torch on the ignition and combustion instability of a cavity flame holder was investigated in this study. Table 2 shows representative DMD modes for Type-A (A-1) and Type-B (B-2). This table presents the fifth dominant DMD mode as observed in the OH* chemiluminescence images. Slight variations are observed near the torch jet orifice. Furthermore, variations are observed within the shear layer. The distribution of DMD modes from near the torch jet orifice to the shear layer is distorted, confirming significant fluctuations in the spatial position of the flame. Such phenomena are also observed in the distribution of OH* chemiluminescence intensity over time, as shown in Fig. 6, indicating unstable combustion regions from the step of the cavity flame holder to the shear layer. Therefore, we conducted a more detailed investigation into the combustion instability within the shear layer based on the analysis results of DMD modes.

Table 2. Representative DMD modes for Type-A (A-1) and Type-B (B-2).

	Mode 1	Mode 2	Mode 3	Mode 4	Mode 5
Type-A (A-1)	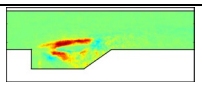	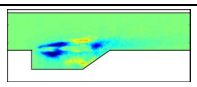	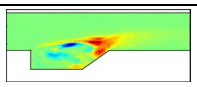	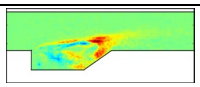	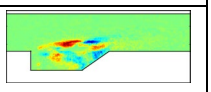
Type-B (B-2)	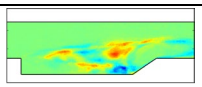	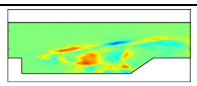	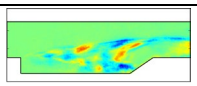	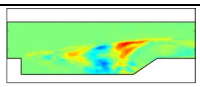	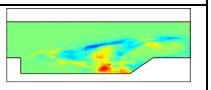

Figure 9 shows the power spectrum density (PSD) of the fast Fourier transform (FFT) based on OH* chemiluminescence images in the shear layer in the case of the Type-A cavity. In this study, the results of the FFT-PSD between the forced ignition and flame holding conditions are compared, as shown in Fig. 9. The reason for comparing the forced ignition and flame holding conditions is that during flame holding, when the torch is stopped, we are able to exclude the influence of combustion oscillations caused by the torch. As shown in Fig. 9 (a), the peaks in the domain are observed at frequencies of 39, 273, 1462, and 2560 Hz in the case of forced ignition for A-1. On the other hand, the peaks in the domain are observed at frequencies of 61, 109, 345, 2013, and 3072 Hz in the case of flame holding for A-1. The peak value changes as the fuel mass flow rate increases. As shown in Fig. 9 (b), the peaks in the domain are observed at frequencies between 15 and 149 Hz, and at 338 and 1120 Hz in the case of forced ignition for A-2. On the other hand, the peaks in the domain are observed at frequencies of 44, 218, 536, and 745 Hz, and between 1579 and 2604 Hz, in the case of flame holding for A-2. Both B-1 and B-2 show numerous peaks in the low-frequency range under forced ignition conditions, whereas under flame holding conditions, many peaks are distributed across the mid to high-frequency range. According to previous studies, oscillations based on frequencies between 100 and 400 Hz were formed

by injector flame feedback, shock flame acoustic feedback, and shock flame acoustic convective feedback [24, 25]. Furthermore, the flow fluctuations around the cavity have relatively low frequencies, suggesting that any periodic shed vortices or acoustic modes do not couple with the reaction zone location oscillation [15]. On the other hand, high frequency oscillations are prone to combustion instabilities and buzz flow in scramjet engines [26]. In addition, according to a previous study, the high-frequency oscillation near the cavity flame holder corresponds to the Rossiter mode, wherein the upstream travelling compression wave reaches the front wall, inducing shed vortices or disturbances, which are subsequently amplified via Kelvin–Helmholtz instability [27]. It is suggested that the amplified structures in the shear layer impinge on the aft wall and generate another compression wave, thus closing the feedback loop [27]. Therefore, in the case of low frequencies between 100 and 400 Hz, fuel injector flame feedback occurred in these combustion results. Furthermore, in the case of low frequencies under 100 Hz (e.g., 15 to 50 Hz), torch gas injector flame feedback occurred in these combustion results. High frequencies greater than 1000 Hz were formed by interference between the cavity flame holder and the flow field. However, it is unclear what kind of flow field occurs near the cavity flame holder during combustion and interferes with the oscillations. Further investigations using numerical analysis will be necessary to elucidate these causes.

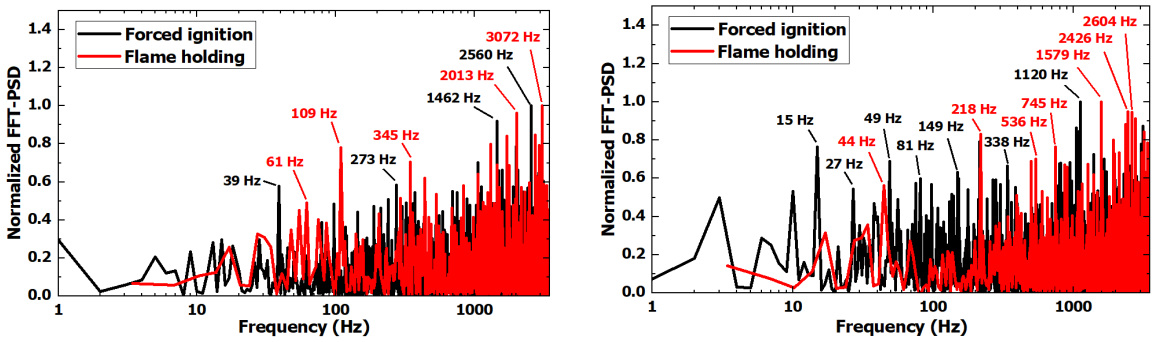

(a) A-1 (b) A-2

Fig 9. PSD of FFT for DMD mode based on OH* chemiluminescence images in the shear layer in the case of type A cavity.

Figure 10 shows the PSD of the FFT based on OH* chemiluminescence images in the shear layer in the case of the Type-B cavity. Similar to the results of the Type-A cavity, the results of the FFT-PSD between the forced ignition and flame holding conditions are compared. In the case of B-1, the peaks during the flame-holding condition are more pronounced than those during the forced ignition condition. As shown in Fig. 10 (a), the peak in the domain is observed at frequency of 2095 Hz in the case of forced ignition for B-1. Multiple peaks are also observed in the range of 50 to 200 Hz in this case. On the other hand, the peaks in the domain are observed at frequencies between 20 and 4650 Hz in the case of flame holding for B-1. In the case of B-2, the difference in peak values between the forced ignition and flame holding conditions is more pronounced than that in B-1. As shown in Fig. 10 (b), the peaks in the domain are observed at frequencies between 39 and 300 Hz, and at frequencies of 657, 1038, 2194, and 2970 Hz, in the case of forced ignition for B-2. On the other hand, the peaks in the domain are observed at frequencies of 11, 53, 77, 107, 709, 1444, and 4272 Hz in the case of flame holding for B-2. In the case of B-3, the distribution of peak values is less pronounced than that under the other conditions. As shown in Fig. 10 (c), the peaks in the domain are observed at frequencies of 32, 46, 852, 2477, 3354, and 4654 Hz in the case of forced ignition for B-3. On the other hand, the peaks in the domain are observed at frequencies between 76 and 624 Hz, and of 14 and 1254 Hz, in the case of flame holding for B-3. In the case of B-4, peaks are observed only in the high-frequency range during the flame holding condition. For example, as shown in Fig. 10 (c), the peaks in the domain are observed at frequencies of 487, 2343, and 4874 Hz in the case of flame holding for B-4. On the other hand, the peaks in the domain are observed at frequencies between 23 and 460 Hz, and of 1411, 2847, and 4417 Hz, in the case of forced ignition for B-4. Therefore, in the case of low frequencies between 100 and 400 Hz, fuel injector flame feedback occurred in these combustion results. Furthermore, low frequencies under 100 Hz (e.g., 20 to 50 Hz) were formed by torch gas injector flame feedback in these combustion

results. However, in the case of B-1, peaks are observed in this low-frequency range (20 to 50 Hz). This is presumed to be influenced by the residual trace gases remaining in the torch after the torch is stopped during flame-holding, which are momentarily expelled into the cavity flame holder. Frequencies greater than 1000 Hz were formed by interference between the cavity flame holder and the flow field. In the case of B-3, where a flame is not formed in the shear layer of the cavity flame holder, the peaks in the high-frequency range are smaller than those under other conditions. This is because, as evident from the OH* chemiluminescence images in Fig. 5(e), the flame is formed from the upper part of the shear layer to the flow passage, and there is little interference between the flow field and the cavity. However, similar to Type-A, it is unclear what kind of flow field occurs near the cavity flame holder during combustion and interferes with the oscillations. Further investigations using numerical analysis will be necessary to elucidate these causes.

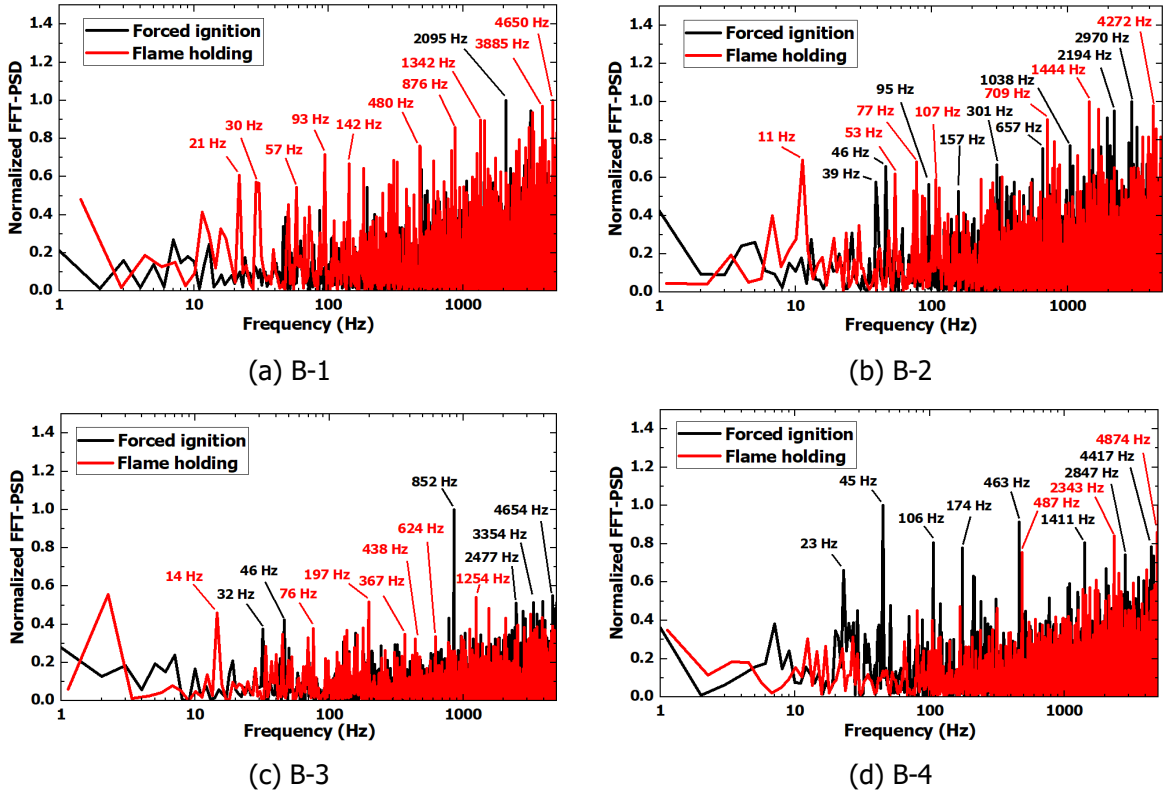

(a) B-1 (b) B-2

(c) B-3 (d) B-4

Fig 10. PSD of FFT for DMD mode based on OH* chemiluminescence images in the shear layer in the case of Type B cavity.

5. Conclusion

In conclusion, this study aimed to investigate the forced ignition and combustion instability mechanisms in a scramjet combustor using modal analysis, particularly Dynamic Mode Decomposition (DMD). The findings revealed significant insights into the combustion process within the cavity flame holder and the shear layer, shedding light on the effects of different fuel mass flow rates on combustion instability. The analysis of OH* chemiluminescence images using DMD provided valuable information about the spatiotemporal dynamics of the combustion process, allowing for a detailed examination of the combustion instability mechanisms. The results highlighted the importance of understanding and mitigating combustion instabilities for the stable operation of scramjet engines. Further research, including numerical analysis, is recommended to deepen our understanding of complex flow phenomena and their interactions in scramjet combustors, ultimately leading to improved engine performance and reliability.

Acknowledgements

This work was supported by JSPS KAKENHI, Grant Number JP23K13496. The author wishes to thank K. Kobayashi and S. Tomioka (Japan Aerospace Exploration Agency, JAXA) for their support and advice during the scramjet combustion experiment at the Kakuda Space Center of JAXA.

References

1. Kobayashi, K., Tomioka, S., Mitani, T.: Supersonic Flow Ignition by Plasma Torch and H_2/O_2 Torch. J. Prop. Power. 20, 294-301 (2004)
2. Ogawa, S., Kobayashi, K., Tomioka, S.: An Experimental Investigation on Forced Ignition Characteristics of Hydrocarbon Mixture Fuel in Scramjet Combustor. Lect. Notes Electr. Eng. 913, 1381-1395 (2023)
3. Ogawa, S., Kobayashi, K., Tomioka, S.: Forced ignition modeling of methane-ethylene mixture in scramjet combustors. Comb. Flame. 263, 113383 (2024)
4. Takita, K., Ohashi, R., Abe N.: Suitability of C_2-, C_3-Hydrocarbon Fuels for Plasma Ignition in High-Speed Flow. J. Prop. Power. 25, 565-570 (2009)
5. Li, F., Yu, X., Tang, Y., Shen, Y., Chen, J., Chen, L., Chang, X.: Plasma-assisted ignition for a kerosene fueled scramjet at Mach 1.8. Aerosp. Sci. Technol. 28, 72-78 (2013)
6. Cuppoletti, D., Ombrello, T., Carter, C., Hammack, S., Lefkowitz, J.: Ignition dynamics of a pulse detonation igniter in a supersonic cavity flameholder. Comb. Flame. 215, 376-388 (2020)
7. Brieschenk, S., Kleine, H., O'Byrne, S.: Laser ignition of hypersonic air-hydrogen flow. Shock Waves. 23, 439-452 (2013)
8. Wang, T., Wang, Z., Cai, Z., Sun, M., Wang, H., Sun, Y., Yang, Y., Li, P., Huang, Y.: Combustion Characteristics in Scramjet Combustor Operating at Different Inflow Stagnation Pressures. AIAA J. 60, 4544-4565 (2022)
9. Poinsot, T., Bourienne, F., Candel, S., Esposito, E., Lang, W.: Supersonic of Combustion Instabilities by Active Control. J. Prop. Power. 5, 14-20 (1989),
10. Taira, K., Brunton, S. L., Dawson, S. T. M., Rowley, C. W., Colonius, T., McKeon, B. J., Schmidt, O. T., Gordeyev, S., Theofilis, V., Ukeiley, L. S.: Modal Analysis of Fluid Flows: An Overview. AIAA J. 55, 4013-4041 (2017)
11. Schmid, P. J.: Dynamic mode decomposition of numerical and experimental data. J. Fluid Mech. 656, 5-28 (2010)
12. Rowley, C. W., Mezic, I., Bagheri, S., Schlatter, P., Henningson, D. S.: Spectral analysis of nonlinear flows. J. Fluid Mech. 641, 115-127 (2009)
13. Nakaya, S., Yamana, H., Tsue, M.: Experimental investigation of ethylene/air combustion instability in a model scramjet combustor using image-based methods. Proc. Comb. Inst. 38, 3869-3880 (2021)
14. Li, X., Lei, Q., Zhao, X., Fan, W., Chen, S., Chen, L., Tian, Y., Zhou, Q.: Combustion Characteristics of a Supersonic Combustor with a Large Cavity Length-to-Depth Ratio. aerospace. 9, 214 (2022)
15. Sethuraman, V. R. P., Yang, Y., Kim, J. G.: Interaction of shock train with cavity shear layer in a scramjet isolator, Phys. Fluids. 35, 036111 (2023)
16. Devaraj, M. K. K., Jutur, P., Rao, S. M. V., Jagadeesh, G., Anavardham, G. T. K.: Investigation of local unstart in a hypersonic scramjet intake at a Mach number of 6, Aerosp. Sci. Technol. 115, 106789 (2021)
17. Nair, P. P., Suryan, A., Narayanan, V.: Modal analysis of mixing characteristics in scramjet combustor with passive struts. Int. J. Hydrog. Energy. 47, 34656-34675 (2022)
18. Takahashi, M., Kobayashi, K., Tomioka, S.: Combustion characteristics of a supersonic combustor model for a JAXA flight experiment. CEAS Space J. 15, 827-844 (2023)

19. Tomioka, S., Hiraiwa, T., Kobayashi, K., Izumikawa, M., Kishida, T., Yamasaki, H.: Vitiation Effects on Scramjet Engine Performance in Mach 6 Flight Conditions. J. Prop. Power. 23, 789-796 (2007)
20. Kutz, J. N., Brunton, S. L., Brunton, B. W., Proctor, J. L.: DYNAMIC MODE DECMOPOSITION Data-Driven Modeling of Complex Systems, Philadelphia (2017)
21. Brunton, S. L., Kutz, J. N.: DATA-DRIVEN SCIENCE AND ENGINEERING Machin Learning, Dynamical Systems, and Control (Second edition), Cambridge (2022)
22. Tu, J. H., Rowley, C. W., Luchtenburg, D. M., Brunton, S. L., Kutz, J. N.: On Dynamic Mode Decomposition: Theory and Applications, J. Comput. Dyn. 1, 391-421 (2014)
23. Xi, J., Zhao, W.: Correlating exhaled aerosol images to small airway obstructive diseases: A study with dynamic mode decomposition and machine learning, PLoS One. 14, (2019)
24. Lin, K. -C., Jackson, K., Behdadnia, R., Jackson, T. A., Ma, F., Yang, V.: Acoustic Characterization of an Ethylene-Fueled Scramjet Combustor with a Cavity Flameholder, J. Prop. Power. 26, 1161-1170 (2010)
25. Nakaya, S., Kinoshita, R., Lee, J., Ishikawa, H., Tsue, M.: Analysis of supersonic combustion characteristics of ethylene/methane fuel mixture on high-speed measurements of CH* chemiluminescence, Proc. Comb. Inst. 37, 3749-3756 (2019)
26. Micka, D. J., Driscoll, J. F.: Combustion characteristics of a dual-mode scramjet combustor with cavity flameholder, Proc. Comb. Inst. 32, 2397-2404 (2009)
27. Wang, H., Wang, Z., Sun, M.: Experimental study of oscillations in a scramjet combustor with cavity flameholders, Exp. Therm. Fluid Sci. 45, 259-263 (2013)